Egy. J. Pure & Appl. Sci. 2024; 62(3):19-32

Egyptian Journal of Pure and Applied Science

Schists of Nuwiba area, southeast Sinai, Egypt: field, petrographic, geochemical and radiometric aspects

Ismail Ahmed Hassan El Akeed

Nuclear Materials Authority, P.O. Box – 530 El Maadi, Cairo, Egypt.

ARTICLE INFO

Received 21 June 2024
Accepted 24 July 2024

Keywords

Schist,
Petrography,
Geochemistry,
Radiometry,
Nuwiba,
Sinai

Correspondence

Ismail Ahmed Hassan El Akeed

E-mail

(Corresponding Author)

elakeed68@gmail.com

ABSTRACT

Nuwiba schists are located at the northernmost segment of the Arabian–Nubian Shield. They occupy two localities in the mapped area situated between Wadi Muqeibila and Wadi Taba. They considered as the oldest rock unit exposed in the mapped area. The schists are derived, by metamorphism of greywackes and pelites or pelitic greywackes sediments. These sediments were originally derived from felsic and intermediate igneous provenance and were deposited in a tectonic setting related to an active continental margin regime. The rocks show limited differences in their major element oxides content suggesting derivation from a common source or provenance, or at least from sources of similar composition. The averages of incompatible trace element patterns in the studied six schist samples compare more to the UCC pattern than the LCC and NASC ones. It is, thus, concluded that the studied metasediments were derived from granitic composition rocks of the upper continental crust. The chondrite-normalized patterns of REE reveal enrichment of the schist in the LREE and their depletion in the HREE with low negative Eu anomalies. The wide range of REE abundance is from 61.48 to 144.87 ppm. suggesting highly fractionated, K-rich granitic rock derivation. The average content of thorium is low but uranium is high relative to the average reported for the argillaceous rocks (Th = 12 and U = 3.7 ppm) due to their derivation origin and epigenetic processes.

1. Introduction

The whole rock geochemistry of Nuwiba schists are frequently used to address the gap in understanding the origin, composition, and geological significance of the schists within the broader context of regional tectonics and geological evolution.

The investigation focuses on delineating the mineralogical and geochemical characteristics, understanding the metamorphic processes, identifying sedimentary protoliths and exploring regional tectonics in Northeast Africa and Southwest Asia.

Additionally, it seeks to determine the provenance and tectonic setting of these metasediments, delineate equilibrium state and mobilization of uranium and assess the implications of these findings for comprehending the geological history of the Arabian–Nubian Shield and regional tectonics.

The Nuwiba area, situated in Southeastern Sinai, represents the northernmost boundary of the Arabian–Nubian Shield and is a segment of the Taba Metamorphic Complex (TMC). This region exemplifies the continental crust underlying Northeast Africa, Southwest Asia, and Arabia, with the eastern part of the shield associated with the Arabian Plate and the western part with the African Plate [1-2]. The studied area covering approximately 60 km² along the western shore of the Gulf of Aqaba, northwest of Nuwiba City, it is bounded by latitudes 29º 22′ 30′′ to 29º 28′ N and longitudes 34º 44′ 45′′ to 34º 54′ E. The K–Ar biotite cooling ages for the TMC, including metapelitic schists, range from 594 to 617 Ma [3]. The initial metamorphic event in the TMC is dated to approximately 620 ± 10 Ma [3-5] reported that the presence of sillimanite porphyroblasts in the metapelitic schists indicates a low-pressure peak metamorphic condition.

Excluding granites, metasediments form the predominant outcropping unit in the Egyptian basement complex. These metasediments are primarily located in the Eastern Desert south of latitude 26º N, with less frequent occurrences north of this latitude and in southern Sinai. They mainly consist of immature clastic and volcaniclastic sediments, ranging from mudstones to conglomerates, and include significant proportions of carbonates, mature sandstones, and cherts with banded iron formations. It is common to find these metasediments intermixed with serpentinites and basic igneous rocks, particularly around large serpentinite masses. Their metamorphic equivalents include slates, schists, greenstones, and, though rarely, amphibolites.

2. FIELD ASPECTS

In the surveyed region, metasediments primarily manifest as schists of diverse compositions. Kröner et al. [7] reported the age of the studied schist ranging between 813 ± 7 to 800 ± 13 Ma. Eliwa et al. [3] identified K–Ar biotite cooling ages ranging from 594 to 617 Ma for the schist under study.

These schists form two belts, one exposed at Wadi El-Morakh, and the other at Wadi Umm Zariq, extending to Wadi Tweiba (Fig. 1). The schists have dark dark grey, greenish grey, and black colors, these rocks exhibit notable foliation and schistosity in the field (Fig. 2a), indicating significant deformation through shearing, folding, and refolding.

Offshoots and apophyses of foliated granitoid intrude these schists, with some xenoliths of schists found within the granitoids, suggesting an older age for the schist. Medium-grained foliated quartz dioritic rocks with sharp, irregular contacts intrude the schist, along with pegmatitic and aplitic granitic dykes of considerable thickness. Garnet porphyroblasts are abundant in the schists, with staurolite found primarily in Wadi Tweiba outcrops, near meta diorites (Fig. 2b). At the entrance of Wadi Tweiba, medium-to-coarse-grained garnet porphyroblast and staurolite crystals are observed. Garnet occurs predominantly in dark bands but is also found in leucocratic veins within the schists, indicating in situ partial melting. Two generations of garnet are noted, with the older one associated with the dark bands and the younger with the leucosome cutting the schistosity. Secondary green copper minerals are observed along fractures in the garnet-staurolite schist. Field investigations reveal multiple types of schists, with a higher abundance of alumino-silicate minerals such as garnet and staurolite, along with remnants of sedimentary bedding, suggesting derivation from alumina-rich sedimentary protoliths (i.e. pelite).

3. MATERIAL AND METHODS

The present study encompasses four primary methodologies, which include fieldwork, petrographical analysis, geochemical investigation, and radiometric examination.

3.1. Fieldwork

Involves the identification, characterization, and mapping of the examined rock formations, as well as the delineation of geological boundaries. Approximately 20 representative manual samples were collected to facilitate diverse analyses, accompanied by the capture of field photographs to document significant observations and features.

3.2. Petrographical study

Entails meticulous petrographic examinations of 20 chosen thin sections representing various rock types. The polarizing microscope was utilized for detailed petrographic assessments.

3.3. Geochemical investigation

Six representative samples underwent chemical analysis employing X-Ray Fluorescence analyses (XRF) methodology to determine major and trace elements such as Rb, Sr, Y, Zr, Nb, and Ba. Additionally, the inductively coupled plasma-atomic emission spectroscopy ICP-AES technique was employed to ascertain the presence of Be, Sc, V, Cr, Co, Ni, Cu, Zn, As, Mo, Ag, Cd, Sn, Sb, W, Pb, U, Th, and Bi, while Rare-Earth Elements REEs were analyzed using inductively coupled plasma-mass spectrometry ICP-MS methodology. These analyses were conducted at the laboratories of the Earth and Atmospheric Sciences Department, Purdue University, USA.

3.4. Radiometric studies

Utilized the calibrated multi-channel spectrometer model RS-230. Employing RS-130 Portable Gamma Spectrometer units equipped with a 6.3 cubic inch Sodium-Iodide detector for Gamma Ray detection, the concentrations of equivalent uranium (U_r) and equivalent thorium (Th_r) in ppm were determined.

4. Results

4.1. Petrography

Regarding petrography, the investigated metasediments are represented by four successive metamorphic zones. Each zone exhibits a specific mineral assemblage that is predominantly evident in the following variations:

4.1.1. Garnet-mica-sillimanite schist

Exhibits foliation and occasional mylonitization, predominantly fine-grained and primarily composed of plagioclase, quartz, biotite, muscovite, and K-feldspars. Accessory minerals include garnet, sillimanite, apatite, sphene, iron oxides, and zircon, while sericite and kaolinite are secondary. Notably, a well-defined schistose texture is evident (Fig. 3a).

Garnet displays indications of replacement by biotite, signifying a subsequent retrograde metamorphism phase [8]. The presence of garnet implies metamorphism reaching the garnet zone of the amphibolite facies. Sillimanite occurs in fibrous aggregates, closely intermixed with biotite and muscovite (Fig. 3b). This assemblage typifies high-grade schist characterized by elevated temperatures prompting muscovite to react with quartz, yielding K-feldspar and sillimanite. Adjacent to fault planes, mylonitization can alter the rocks to various degrees of crushing.

4.1.2. Cordierite-biotite schist

Fine to medium-grained with distinct schistosity, primarily comprising biotite, plagioclase, and quartz. Accessory minerals encompass hornblende, orthoclase, garnet, cordierite, zircon, and apatite. Biotite, reddish-brown, tends towards parallel orientation with other constituents (Fig. 3c). Cordierite forms small subidioblastic grains, corroding biotite flakes and partly growing at their expense, indicative of its later formation. Cordierite's presence suggests Mg sourced from biotite decomposition and alteration to chlorite, consistent with previous interpretation of [9, 10].

4.1.3. Garnet-biotite schist

Grey, medium-grained with well-defined foliation, displaying a medium-grained granoblastic texture, primarily comprising biotite, plagioclase, quartz, and garnet. Iron oxides and sericite constitute main accessories. Biotite occurs as medium-grained subidiomorphic flakes, sometimes altered to chlorite, indicating retrograde metamorphism. Three generations of garnet were observed (Figs. 3d, 3e & 3f).

4.1.4. Andalusite-garnet-biotite schist

Composed mainly of plagioclase, biotite, quartz, garnet, K-feldspars, andalusite, and muscovite. Chlorite, sericite, kaolinite, and carbonates are secondary, with apatite, sphene, and zircon as accessories. Biotite exhibits wavy extinction and curved cleavages due to deformation effects, while garnet occurs as equidimensional crystals, displaying a wide variation in grain size. The genesis of garnet can be explained according to the following reaction: Chlorite + biotite (Fe–Mg) + quartz = garnet + biotite (Mg–Fe) +H_2O, [11, 12]. Andalusite porphyroblasts, showing sector twinning, contain numerous inclusions, forming a poikiloblastic texture, and oriented parallel to the foliation (Figs. 3g & 3h).

4.2. Geochemistry

The investigation into the geochemistry of the presented schists involved the analysis of six representative samples with varying textures and compositions for their major oxides, trace elements, and Rare Earth Elements (REE), the results of which are presented in Table 1.

4.2.1. Major Oxides

These schists are typified by intermediate silica content, averaging 64.18%. With the exception of sample no. 1, there is notable uniformity in SiO_2, TiO_2, Al_2O_3, MnO, MgO, and P_2O_5 contents across samples, while CaO, Na_2O, and K_2O exhibit limited variation ranges (Fig. 4a).

Comparisons of the average values of the major oxides with some averages from the published literature (Table 2) are displayed in Fig. 4b.

4.2.2. Trace Elements Geochemistry

Comparison of the averages of incompatible trace elements in the six schist samples with upper continental crust (UCC) from Taylor and McLennan [13], lower continental crust (LCC) from Weaver and Tarney [14] and North American Shale Composition (NASC) from Gromet et al. [15] plotting on a multi-element spider diagram (Fig. 4c).

Normalization to the UCC, LCC and NASC average values plotted on another spider diagram (Fig. 4d) and Data on trace elements characteristic of basic rocks compared to UCC and NASC averages plotted in Fig. 4e.

4.2.3. Rare Earth Elements (REE) Geochemistry

Normalization of REE data to average chondrite values of Evensen et al. [16] reveals enrichment in Light Rare Earth Elements (LREE) and depletion in Heavy Rare Earth Elements (HREE), with Ce/Yb ratios ranging from 4.43 to 8.22 and average Eu/Eu* ratios indicating low negative anomalies (Fig. 4f). Total REE abundance varies from 61.48 to 144.87 ppm. The data were also normalized to the NASC values [15] as displayed in Fig 4g.

4.3. Radiometry

The investigated rocks exhibit diverse mineralogical compositions, resulting in a wide variation in their radioelement contents, which were assessed both radiometrically and chemically, alongside their parameters and ratio values (Table 3). These relationships are visually depicted in Figure 5a. Field radiometric measurements indicate that equivalent uranium (U_r) ranges from 3 to 10 ppm, averaging at 7.33 ppm, while equivalent thorium (Th_r) ranges from 5 to 15 ppm, with an average of 9.5 ppm. Chemically determined uranium (U_c) spans from 3.1 to 7.3 ppm, with an average of 5 ppm, whereas measured thorium (Th_c) ranges from 4.8 to 13.8 ppm, averaging at 7.75 ppm. Notably, the average uranium content is relatively high compared to the reported average for argillaceous rocks (3.7 ppm) [17]. The Th_c/U_c and Th_r/U_r ratios exhibit low values, ranging from 1.29 to 2.42 with an average of 1.54 and from 0.56 to 2.67 with an average of 1.43, respectively. Additionally, the ratio between chemically determined uranium (U_c) and radiometrically measured uranium (U_r) in the studied schist (U_c/U_r) ranges from 0.34 to 1.37, averaging at 0.8.

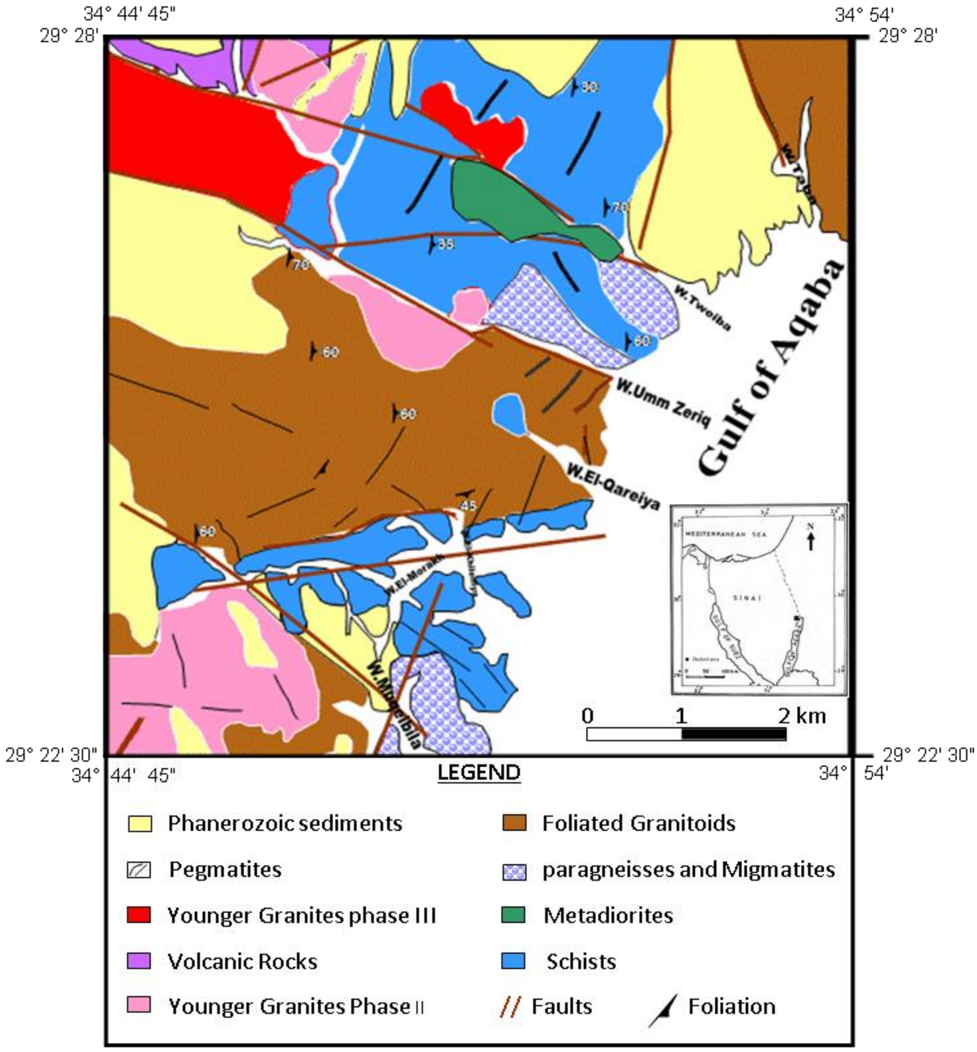

Fig. 1 Location and geologic maps of Nuwiba area, southeastern Sinai, Egypt.

Fig.2a Well-developed schistosity in the schist.Wadi Umm Zeriq.

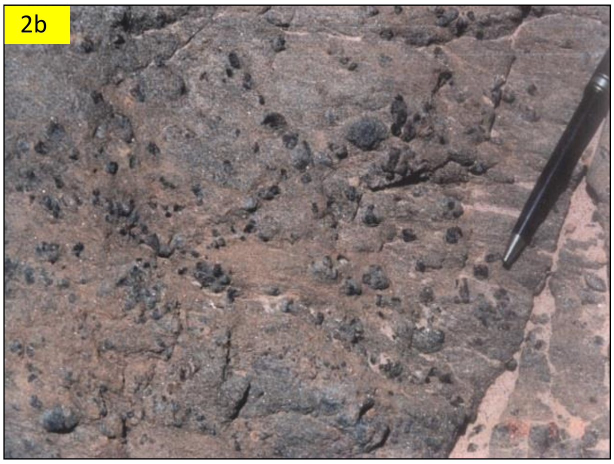

Fig. 2b Garnet-staurolite schist showing porphyroblasts of garnet and staurolite, Wadi Tweiba.

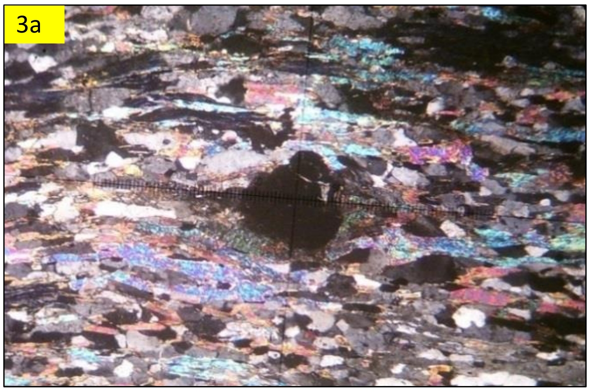

Fig. 3a A photomicrograph for a garnet-mica-sillimanite schist showing well developed schistose texture and preferred orientation of muscovite, biotite and elongated quartz grains. Crossed polars (C. P.), X 10.

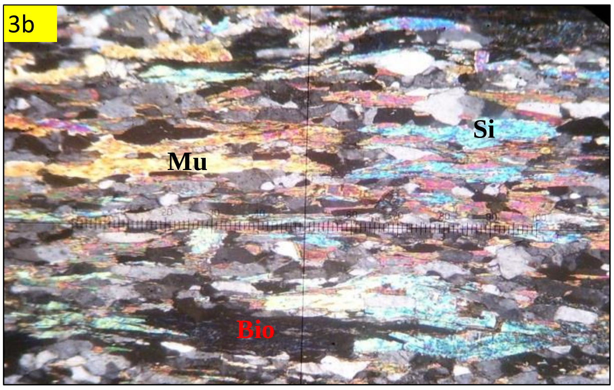

Fig. 3b A photomicrograph for a garnet-mica- sillimanite schist showing fibrous sillimanite (Sil) associated with biotite (Bio) and muscovite flakes (Mus). C. P., X. 10.

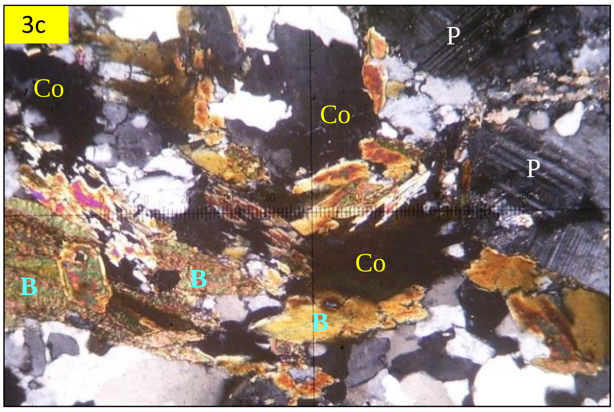

Fig. 3c A photomicrograph for a cordierite-biotite schist showing twinned plagioclase (Pl), cordierite (Cor) and parallel orientation of biotite (Bio). C. P., X. 10.

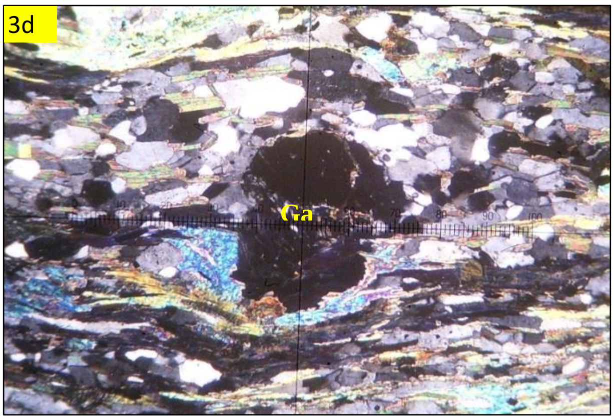

Fig. 3d A photomicrograph of garnet-biotite schist showing idioblastic pre-tectonic garnet (Gar) porphyroblasts. C. P., X. 10.

Table 1. Major oxides (Wt %), trace elements (ppm) and REEs Data of Nuwiba schists.

M. Oxdes	1	2	3	4	5	6	Average
SiO_2	72.86	62.9	59.4	62.9	65.1	61.9	64.18
TiO_2	0.21	0.81	0.89	0.79	0.69	0.7	0.68
Al_2O_3	15.1	16.6	17.9	17.1	16.96	16.5	16.69
Fe_2O_3	3.1	6.61	8.23	5.81	5.27	6.32	5.89
MnO	0.12	0.18	0.17	0.15	0.14	0.11	0.15
MgO	1.29	2.91	3.41	3.1	2.21	2.28	2.53
CaO	1.24	2.97	2.16	2.31	2.89	2.68	2.38
Na_2O	3.46	3.62	3.52	2.46	3.84	3.98	3.48
K_2O	2.13	2.25	2.71	3.42	2.1	3.54	2.69
P_2O_5	0.12	0.19	0.18	0.26	0.21	0.28	0.21
LOI	0.8	1.14	1.5	1.7	0.8	1.9	1.31
Sum	100.43	100.18	100.07	100	100.21	100.19	100.19
Trace Es.							
Be	2.8	1.7	1.6	2.9	2.1	1.9	2.17
Sc	2.7	10	19.98	12.5	8.1	10.8	10.68
V	11	79	149	95	59	89	80.33
Cr	152	224	247	179	183	214	199.83
Co	9	18	30	19	17	21	19
Ni	10	51	71	63	31	34	43.33
Cu	9.8	41.4	19.8	9.1	12.9	10.3	17.22
Zn	57	168	141	112	121	129	121.33
As	<3	<3	5	69	8	9	22.75
Rb	102	63	79	117	63	71	82.5
Sr	398	370	241	351	489	248	349.5
Y	<2	28	33	25	21	26	21.67
Zr	82	181	164	172	151	185	155.83
Nb	8	7	10	9	8	8	8.33
Mo	3	3	3	6	4	<1	3.25
Ag	0.3	<0.2	0.7	0.9	0.4	0.3	0.317
Cd	<1	<1	2	2	2	<1	1
Sn	<10	<10	<10	<10	<10	<10	<10
Sb	9	<5	12	8	7	9	7.17
Ba	671	600	611	998	556	597	672.17
W	<10	<10	<10	<10	<10	<10	<10
Pb	17	11	7	18	12	9	12.33
Bi	<5	<5	<5	<5	<5	<5	<5
U	3.1	7.3	5.7	5.7	4.1	4.1	5
Th	4.8	9.4	7.5	13.8	5.7	5.3	7.75
REEs							
La	13.7	24.8	25.9	31.1	21.2	23	23.28
Ce	22.9	44.3	56.4	56.2	40.6	51.1	45.25
Pr	3.1	5.7	5.9	5.4	4.5	4.6	4.87
Nd	11.2	24	27.9	25.1	19.1	21.4	21.45
Sm	2.9	5.7	6.7	5.3	4.6	4.8	5
Eu	0.47	1.58	1.36	1.67	1.17	1.4	1.275
Gd	2.4	5.2	6.1	5.1	3.9	4.8	4.58
Tb	0.3	0.8	0.9	0.8	0.5	0.7	0.67
Dy	1.8	4.9	5.6	4.3	3.9	4.1	4.1
Ho	0.46	1.03	1.11	0.95	0.88	0.86	0.88
Er	1.2	3.4	3.7	2.6	2.7	2.8	2.73
Tm	0.2	0.4	0.5	0.4	0.3	0.3	0.35
Yb	0.7	2.3	2.3	3.1	2	2.9	2.217
Lu	0.15	0.39	0.5	0.42	0.32	0.31	0.35
ΣREE	61.48	124.5	144.87	142.44	105.67	123.07	117.002

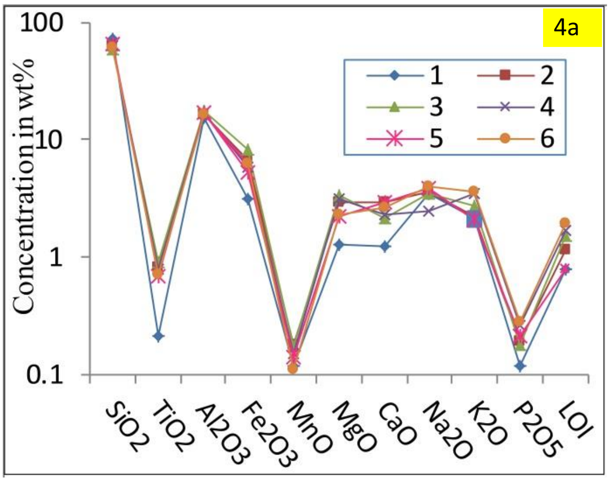

Fig. 4a Comparison of Nuwiba schists major oxides.

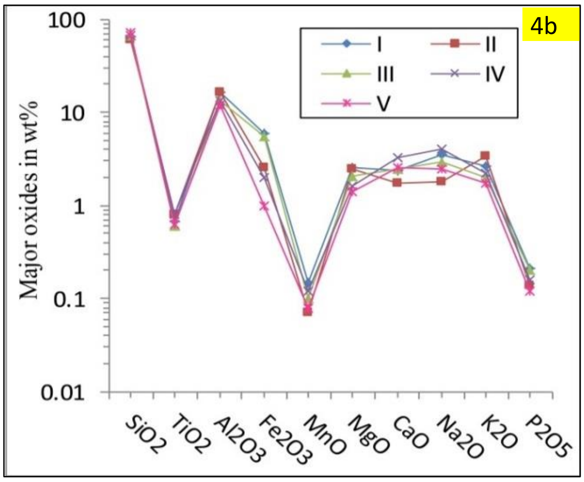

Fig.4b Comparison of Nuwiba schist average major composition with some Egyptian and international schists averages as reported in table **2**.

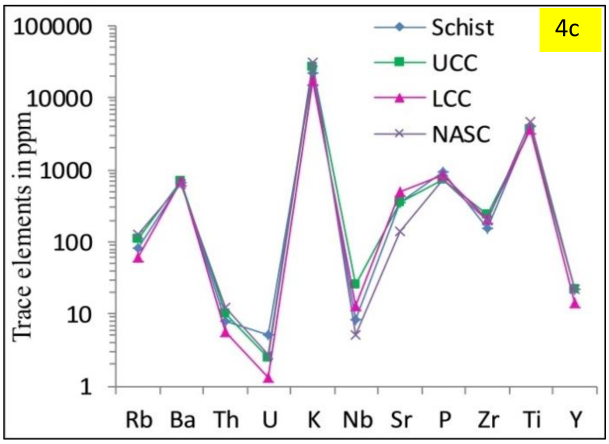

Fig. 4c Comparison of incompatible trace element average abundance in studied schists with their average abundances in upper continental crust (UCC), lower continental crust (LCC) and North American Shale Composition (NASC).

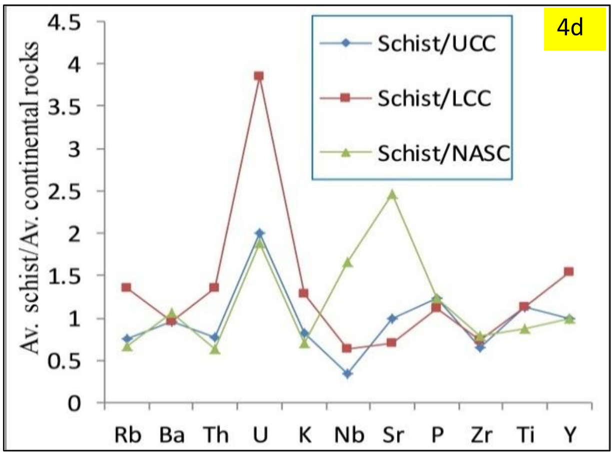

Fig. 4d Normalized trace elements patterns of studied schists average to upper continental crust (UCC), lower continental crust (LCC) and North American Shale Composition (NASC).

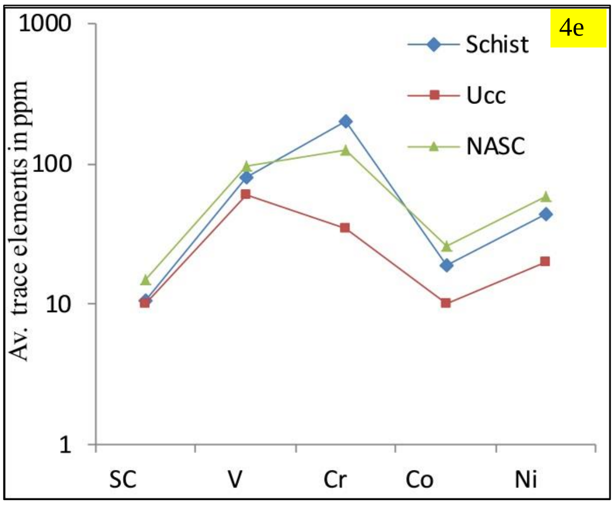

Fig. 4e. Compatible trace element concentration normalized to upper continental crust (UCC) and North American Shale Composition (NASC) averages, Nuwiba schists.

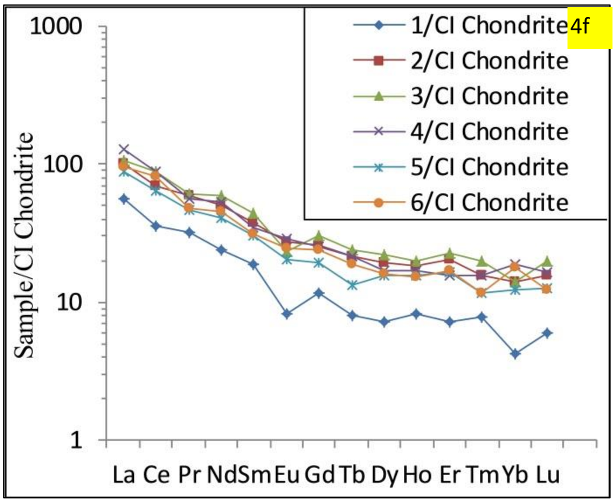

Fig. 4f REE patterns for Nuwiba schists samples normalized to chondrites [16] .

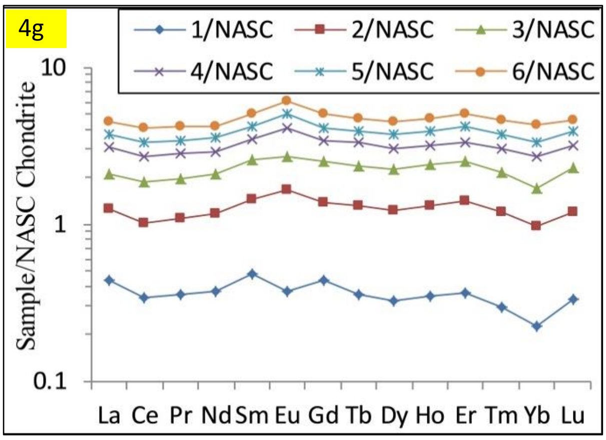

Fig. 4g REE patterns for Nuwiba schists samples normalized to North American Shale Composition (NASC).

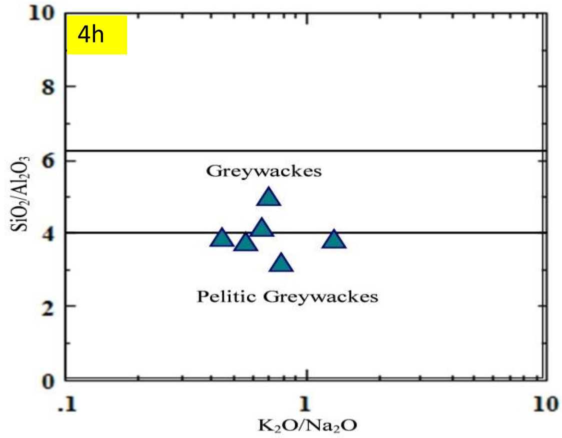

Fig. 4h $SiO_2/Al_2O_3 – K_2O/Na_2O$ Discrimination diagram [24].

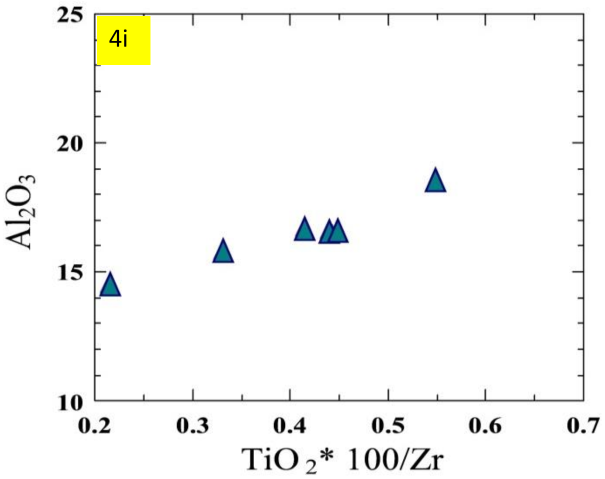

Fig.4i Al_2O_3 -TiO_2*100/Zr variation diagram for the studied schists [25].

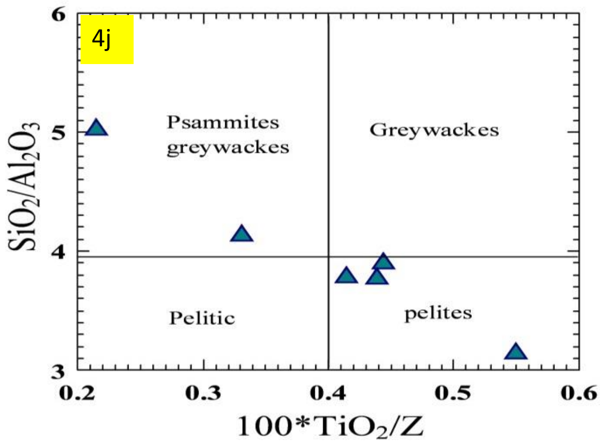

Fig.4j SiO_2/Al_2O_3 - 100*TiO_2/Zr variation diagram for the studied schists [25].

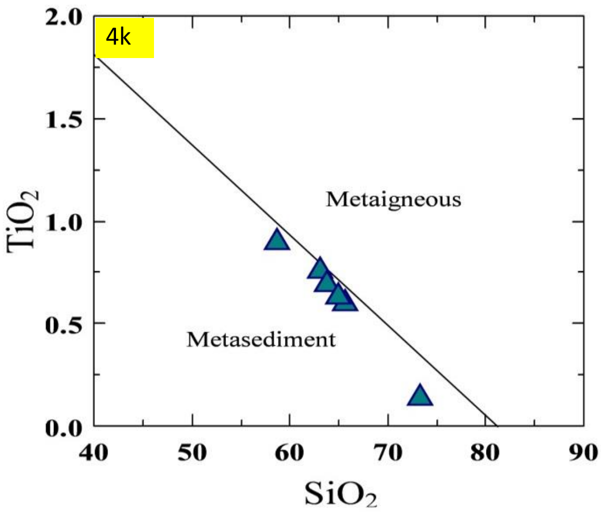

Fig.4k $TiO_2 – SiO_2$ diagram [26].

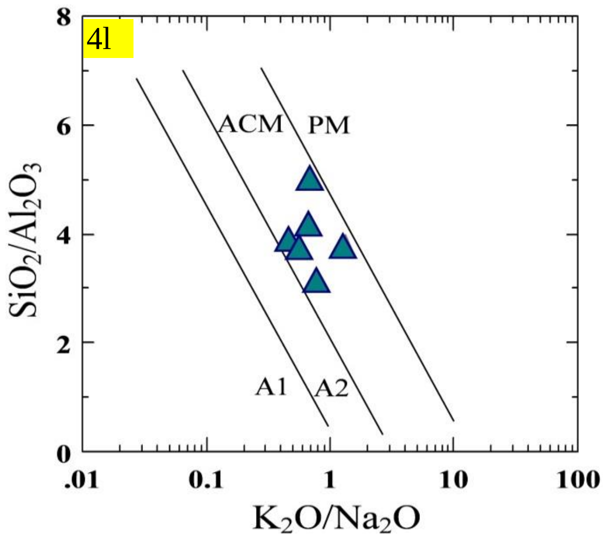

Fig.4l $SiO_2/Al_2O_3 – K_2O/Na_2O$ relationship of the studied schists [27]. A1 = arc setting basaltic andesitic detritus; A2 = evolved arc setting, plutonic Felsic – plutonic detritus; ACM = active continental margin, PM = Passive margin.

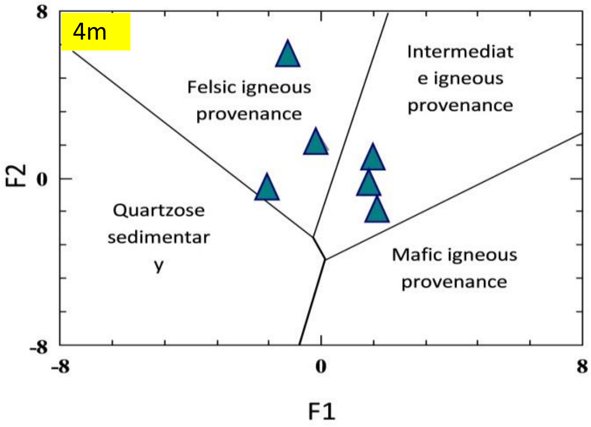

Fig.4m Tectonic discrimination function diagram for the studied schists using major elements [28].

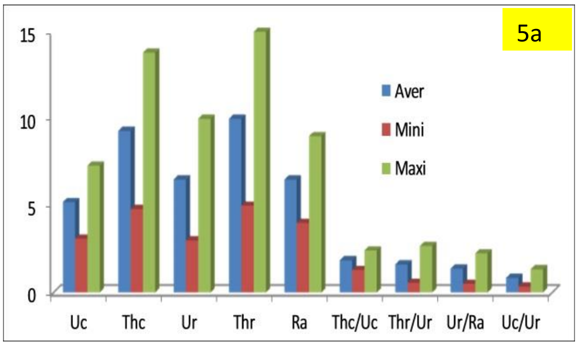

Fig. 5a Histogram shows maximum, minimum and averages of chemical uranium and thorium measuring (U_c & Th_c) and radiometric uranium and thorium (U_r &Th_r) measuring in ppm and their ratios.

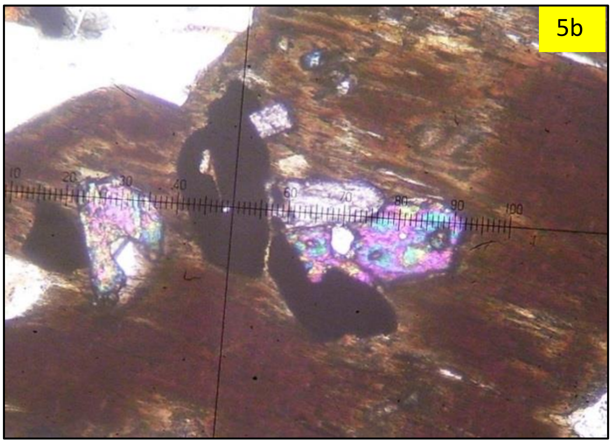

Fig 5b A photomicrograph for Zircon incorporated within biotite with surrounding pleochroic halos related to the radioactive elements content. C. P., X. 20.

Table 2. Comparison of average chemical composition of Nuwiba schists with some Egyptian and international world averages.

S/No.	I	II	III	IV	V
SiO_2	64.18	60.76	66.7	66.87	71.66
TiO_2	0.68	0.81	0.6	0.79	0.63
Al_2O_3	16.69	16.73	13.5	13.55	11.8
Fe_2O_3	5.89	2.53	5.49	2	1
MnO	0.15	0.07	0.1	0.12	0.08
MgO	2.53	2.49	2.1	1.64	1.43
CaO	2.38	1.74	2.5	3.27	2.54
Na_2O	3.48	1.82	2.9	4.04	2.43
K_2O	2.69	3.41	2	2.23	1.73
P_2O_5	0.21	0.14	0.2	0.16	0.12

I - Average of the studied schists.
II - Average of pelite [18].
III - Average of greywacke [19].
IV - Average of biotite schist of Wadi Hafafit area [21].
V - Average of Hill In Endsuite greywackes (Continental Island arc) [20].

Table 3. U_c, Th_c, U_r, Th_r, Ra, contents and radiometric ratios for Newiba Schist.

	S.No.	Chemical analyses		Gamma ray spectrometry			Radiometric ratios			
		U_c	Th_c	U_r	Th_r	Ra	Th_c/U_c	Th_r/U_r	U_r/Ra	U_c/U_r
Nweiba Schists	1	3.1	4.8	9	15	9	1.55	1.67	1	0.34
	2	7.3	9.4	8	8	7	1.29	1	1.1	0.91
	3	5.7	7.5	5	6	4	1.32	1.2	1.3	1.14
	4	5.7	13.8	10	15	6	2.42	1.5	1.7	0.57
	5	4.1	5.7	9	5	4	1.39	0.56	2.3	0.46
	6	4.1	5.3	3	8	6	1.29	2.67	0.5	1.37
	Aver	5	7.75	7.33	9.5	6	1.54	1.43	1.3	0.8
	Mini	3.1	4.8	3	5	4	1.29	0.56	0.5	0.34
	Maxi	7.3	13.8	10	15	9	2.42	2.67	2.3	1.37

5. Discussion

5.1. Field Aspect and Petrography

The mineral assemblage observed in the Nuwiba schists suggests their derivation from Al-rich pelite protoliths that underwent extensive metamorphism in the amphibolite facies.

5.1.1. Trend of the Metamorphic Intensity of the Studied Nuwiba Schists

The rise in anorthite content of plagioclase from south to north. Development of ribbon texture in the northern Nuwiba schists. - First appearance of cordierite, andalusite, sillimanite, and garnet towards the northern extent. - Gradual enlargement of metamorphic mineral porphyroblasts, indicating elevated temperature (Fig. 2b). An increase in metamorphic grade is evident from south to north across the Nuwiba schists, manifested by several observations: - Gradual decrease in sphene and epidote content from south to north, reflecting increased metamorphic grade.

5.1.2. Metamorphic History

Polyphases of metamorphism influencing the Nuwiba schists are explained as follows: - Regional Metamorphism: Medium-grade regional metamorphism occurred within the amphibolite facies, confirmed by the mineral assemblage of hornblende, biotite, quartz, and epidote. Subsequent pressure and temperature increases led to high-grade metamorphism, marked by the presence of garnet and sillimanite. - Thermal Metamorphism: Likely associated with granitoid intrusions, thermal metamorphism elevated temperatures, leading to ribbon texture development, biotite replacement by sillimanite, and enlargement of garnet porphyroblasts near granitoid contacts.

- Retrograde Metamorphism: Following regional and thermal metamorphism, retrograde metamorphism ensued, indicated by the replacement of higher index minerals such as garnet by biotite (Fig. 3d). - Dynamic Metamorphism: Post-regional and thermal metamorphism, Nuwiba schists underwent significant strain effects typical of dynamically metamorphosed rocks, including bending of mica cleavages and plagioclase lamellae, dislocation of plagioclase lamellae, development of undulatory extinction in quartz, and breakage of grains, particularly non-ductile minerals like feldspar.

5.2. Geochemistry

The major oxides consistency of studied schists suggests a shared source or provenance, with the disparity in sample no. 1 attributed to lower weathering degrees and distinct feldspar compositions. Comparative analysis with published literature averages (Table 2 & Fig. 4b) reveals more or less similarities to average of pelite [18] and greywackes [19] though with higher Al_2O_3 and Na_2O and lower SiO_2. Notably, they differ significantly from Hill Endrite greywackes [20] but align closer to biotite schist averages from the Wadi Hafafit area [21].

Comparison of the averages of incompatible trace elements patterns suggests closer resemblance to the UCC pattern (Fig. 4c). Normalization to UCC averages yields smoother variations, indicating derivation from a source akin to UCC composition (Fig. 4d). Notably, elements such as Th, Y, Zr, Nb, Ti, P, and Sc demonstrate minimal variability, suggesting derivation from upper continental crustal rocks, primarily granitic in composition.

It also conforms with a statement by McLennan et al. [22]. Conversely, elements like Rb, Ba, U, and K exhibit greater variability. Data on trace elements characteristic of basic rocks compared to UCC and NASC averages indicate a closer alignment with UCC composition (Fig. 4e). The wide range abundance of total REE and Eu depletion suggest that the schists are derived from highly fractionated, K-rich granitic rocks [13, 23]. Normalization to NASC values [15] corroborates these findings, supporting the conclusion of a granitic provenance for these metasediments (Fig. 4g). Notably, sample 1 displays a distinctive pattern, albeit following the general trend, with lower REE abundances.

5.2.1. Protolith Nomenclature

Preservation of original bedding in the studied schists unequivocally confirms their metamorphosed sedimentary origin. The compositional diversity, discerned from the SiO_2/Al_2O_3 vs. K_2O/Na_2O discrimination diagram (Fig. 4h) [24], places the analyzed samples within the compositional fields of greywackes, indicating a contribution from some mafic components.

Furthermore, positive correlation between $A1_2O_3$ percentages and $100TiO_2/Zr$ (Fig. 4i), characteristic of clastic sedimentary rocks (greywackes) [25]. and distinction between pelite and psammite sedimentary rocks (greywackes) based on TiO_2/Zr vs. $SiO_2/A1_2O_3$ diagram (Fig. 4j) [25] further supports the sedimentary origin of the Nuwiba schists. Additionally, analysis using TiO_2 vs. SiO_2 plot (Fig. 4k) [26] suggests that most studied schist samples are at the border of the metasedimentary field, influenced by both "igneous source" chemistry and processes that led to a "sedimentary parentage."

5.2.2. Tectonic Setting

Based on plate tectonic concepts, the studied schists are indicative of deposition in a basin adjacent to an active continental margin setting, as suggested by their plot in the ACM field on the SiO_2/Al_2O_3 vs. K_2O/Na_2O discrimination diagram (Fig. 4l) [27]. Furthermore discrimination function diagram analysis (Fig. 4m) [28] suggests that the Nuwiba schists likely originated from intermediate to felsic igneous provenance fields, with scatter in plots attributed to grain size, mineral segregation, and metamorphism.

5.2. Radiometry

The relationship between uranium (U) and thorium (Th), along with their ratios, reflects uranium remobilization associated with solution circulation. [29] defined the equilibrium factor as the ratio between chemically determined uranium (Uc) and radiometrically measured uranium (Ur), denoted as the D-factor (D = Uc/Ur). Equilibrium is achieved if this factor equals unity.

Deviations from unity indicate uranium addition or removal [29, 30]. In the Nuwiba schist, the Uc/Ur ratio ranges from 0.34 to 1.37, averaging 0.8 (Table 3), indicating disequilibrium. The coherent behavior of U and Th is a widely accepted hypothesis, with Th considered immobile under similar conditions to U, leading to spatially exogenic uranium redistribution and heterogeneous Th/U or U/Th ratios within the geological body [31]. In the Nuwiba schist, all calculated ratio values indicate uranium remobilization and disequilibrium. High immobile thorium content, coupled with heterogeneous and anisotropic uranium distribution, suggests a syngenetic origin. However, epigenetic processes, especially intrusion by younger granites, significantly contribute to uranium remobilization. Uranium and thorium elements measured in the schist may be incorporated into observed accessory minerals such as apatite and zircon, the latter often found within biotite with surrounding pleochroic halos (Fig. 5b).

6. Conclusion

The Nuwiba schists form two belts in the mapped area, characterized by fine-to-medium-grained, dark grey, greenish-grey, and black coloration, indicative of significant deformation evidenced by shearing, folding, and refolding. Abundant garnet porphyroblasts in various sizes suggest derivation from high-alumina sedimentary protoliths (pelites).

Petrographically, the studied metasediments are categorized into four varieties based on mineral assemblage content: garnet-mica-sillimanite schist, cordierite-biotite schist, garnet-biotite schist, and andalusite-garnet-biotite schist.

Geochemically, the schists exhibit intermediate silica content and limited variations in major oxide content, suggesting a common source or provenance with similar composition. Comparison of incompatible trace element averages with upper continental crust (UCC), lower continental crust (LCC), and North American Shale Composition (NASC) on a multi-element spider diagram shows closer resemblance to the UCC pattern, indicating derivation from source(s) similar in composition. Chondrite-normalized patterns reveal LREE enrichment, HREE depletion, and low negative Eu anomalies, characteristic of clastic sedimentary rocks (greywackes) deposited in a basin adjacent to an active continental margin.

Chemical analysis and radiometric measurements of the radioelements within the Nuwiba schist unveil uranium disequilibrium and remobilization.

8. References

1. **Jia-Horng., K., & Ding-Shinn., C. (2018).** Hepatitis B virus and liver disease. Springer Nature Singapore Pte Ltd.
2. **Gerok., W., Huber., C., Meinertz., T., & et al. (2000).** Die Innere Medizin, 10th ed. Schattauer, F.K. Verlag.
3. **Samuel., SO., Aderibigbe., SA., Salami., TAT., & Babatunde., OA. (2009).** Health workers' knowledge, attitude and behavior towards hepatitis B infection in South Nigeria. International Journal of Medicine and Medical Sciences, **1(10): 418-424.** https://academicjournals.org/journal/IJMMS/article-full-text-pdf/2E977A741.
4. **World Health Organization. (2023).** Hepatitis B. https://www.who.int/news-room/fact-sheets/detail/hepatitis-b
5. **Lavanchy., D. (2004).** Hepatitis B virus epidemiology, disease burden, treatment, and current and emerging prevention and control measures. J Viral Hepat **11(2): 97-107.** https://pubmed.ncbi.nlm.nih.gov/14996343/
6. **Geue., C., Wu., O., Xin., Y., Heggie., R., Hutchinson., S., Martin., N K., & et al. (2015).** Cost-effectiveness of HBV and HCV screening strategies – a systematic review of existing modelling techniques. PLoS One **10(12):e0145022.** https://journals.plos.org/plosone/article?id=10.1371/journal.pone.0145022.
7. **World Health Organization. (2017).** Guidelines on hepatitis Band C testing. **ISBN 978-92-4-154998-1.** https://iris.who.int/bitstream/handle/10665/254621/9789241549981-eng.pdf.
8. **Ekins., RP. (1974).** Basic Principles and Theory: Radioimmunoassay and saturation analysis. Brit Med Bull **30:3-11.** https://academic.oup.com/bmb/article-abstract/30/1/3/307721.
9. **Schwarz., S. (1982).** Radioimmunoassay and related procedures in medicine. IAEA, Vienna, **447.** https://www.iaea.org/publications/3460/radioimmunoassay-and-related-procedures-in-medicine-1982-vienna-21-25-june-1982.
10. **Taravt., B., & Atefeh., Y. (2022).** Hepatitis Viruses. Encyclopedia of infection and immunity, **2: 113-122.** https://www.sciencedirect.com/science/article/abs/pii/B9780128187319000781?via%3Dihub.
11. **Hany., M., Shouman., S., El-Bayoumy., A., Abdel Mohty., A., Mehany., N., & Gado., M. (2021).** Preparation and purification of HBsAg from HBsAg-positive human blood. Egypt J Rad Sci Applic **34(1): 117-120.** https://ejrsa.journals.ekb.eg/article_238970_01f002f26c3fe76eca67b1d8708bc265.pdf.
12. **Lim., KJ., Oh., JH., Shon., V., Yoo., SB., Lee., SI . (2003).** Diagnostic reagents and methods for antibody against hepatitis Bsurface antigen and for antibody against hepatitis B virus. U.S. Patent Application No. 10/181,430. https://patents.google.com/patent/US20030032008A1/en.
13. **Reuschel., V., Jilg., W., Seelbach-Goebel., B., & Deml., L. (2019).** Comparative purification and characterization of hepatitis B virus-like particles produced by recombinant vaccinia viruses in human hepatoma cells and human primary hepatocytes. PLOSONE **14(2): e0212800.** https://journals.plos.org/plosone/article?id=10.1371/journal.pone.0212800.
14. **Gasser., B., and Mattanovich., D. (2019).** Recombinant protein production in yeast, methods in molecular biology. Humana Press.

15. **Michel., ML., Mancini., M., Sobczak., E., Faviert., V., Guetardt., D., Bahraouit., EM., & Tiollais., P. (1988)**. Induction of anti-human immunodeficiency virus (HIV) neutralizing antibodies in rabbits immunized with recombinant HIV-hepatitis B surface antigen particles. Proc Natl Acad Sci USA **85: 7957-7961.** https://www.pnas.org/doi/abs/10.1073/pnas.85.21.7957.
16. **Rao., PN., and Moore., PH. (1977).** Synthesis of new steroid haptens for radioimmunoassay. Part IV: 3-O-carboxymethyl ether derivatives of estrogens. Specific antisera for radioimmunoassay of estrone, estradiol-17β, and estriol. Steroids, **29:461-469.** https://www.sciencedirect.com/science/article/abs/pii/0039128X77900666.
17. **Mineo., CD., Donald., IC., Michael., SM., Cathy., O. (1973).** Production and properties of antisera to dexamethasone- protein conjugates. Biochem J, **133: 401-404.** https://www.ncbi.nlm.nih.gov/pmc/articles/PMC1177713/.
18. **Hope., PC., Laird., CW., & Fox., RR. (1969).** A simple technique for bleeding the rabbit's ear vein. Lab Anim Care, **19: 524-532.** https://pubmed.ncbi.nlm.nih.gov/4240736/.
19. **Kaplan., HM., & Timmons., EH. (1979).** The Rabbit: a model for the principles of mammalian physiology and surgery. Academic Press, New York.
20. **Chapman., RS. (1998).** Radiolabelling for immunoassay. No. IAEA-TECDOC-1001, Austria, **pp39-55.**
21. **Pillai., MRA., & Bhandarkar., SD. (1998).** Radioimmunoassay, principles and practice, 3rd edn. Isotope Division Bhabha Atomic Research Center, Mumbai, India **pp 40–98.**
22. **Roada., ESJ., Kaptein., E., Loonland., MAC., Vanlon., MA., & Vifsar., K. (1988).** Development of Radioimmunoassay for Triiodothyronine Sulfate. J Immunol, **9: 125-137.** https://www.tandfonline.com/doi/abs/10.1080/15321818808057036.
23. **Scatchard., G. (1949).** The attraction of proteins for small molecules and ions. Ann N Y Acad Sci J, **51(4): 660-672.** https://nyaspubs.onlinelibrary.wiley.com/doi/10.1111/j.1749-6632.1949.tb27297.
24. **Mikkelsen., SR., & Corto´n., E. (2016).** Bioanalytical chemistry (2nd ed). John Wiley & Sons Ltd, **86-127.**
25. **Law., B. (2005).** Immunoassay a practical guide. Taylor &Francis e-Library, **12- 192.**
26. **Kar., A. (2005).** Pharmaceutical drug analysis, 2nd edition. New Age International (P) Ltd, **pp 485-509.**
27. **Mehany., NL., El Kolaly., MT., Meky., NH., & Ebeid., NH. (2009).** Preparation of liquid phase-double antibodies radioimmunoassay for the in vitro determination of prolactin hormone in human serum. Isotope and Radiation research, **41(4s2): 1403-1419.** https://inis.iaea.org/Search/search.aspx?orig_q=RN:41122972.
28. **Quiroga., JA., Gonzalez., O., Carreno., V., Mora., I., Porres., JC., Gutiez., J., Hemandez-Guio., C. (1985).** Radioimmmunoassay for detecting hepatitis B core antigen in serum from patients with chronic hepatitis B infection. Clinical Chemistry, **31(6): 831-834.** https://academic.oup.com/clinchem/article-abstract/31/6/831/5651617.
29. **Feldkamp., CS. (1992).** Evaluation and clinical validation of immunoassays. In: Nakamura RM, Kasahara Y, Richnitz GA (Eds.), Immunochemical assays and biosensor technology for the 1990's. Washington D. G., American Society of Microbilogy, **pp 96-109.**
30. **Lamontagne., RJ., Bagga., S., & Bouhard., MJ . (2016).** Hepatitis B virus molecular biology and pathogenesis. Hepatoma Research **2: 163-186.** https://pubmed.ncbi.nlm.nih.gov/28042609/.
31. **Kew., MC. (2012).** Hepatitis B virus / human immunodeficiencyvirus co-infection and its hepatocarcinogenic potential in Sub-Saharan black Africans. Hepat Mon 12(10 HCC): **e7876.** https://www.ncbi.nlm.nih.gov/pmc/articles/PMC3500827/.

32. **CDC. (2023).** Screening and testing recommendations for chronic hepatitis B virus infection (HBV). https://www.cdc.gov/hepatitis/hbv/testingchronic.htm
33. **Chen., EM., and Kasturi., SS. (2010).** DEJA Review™ microbiology and immunology, 2nd edition. Mc Graw-Hill.
34. **Sanders., ER. (2012).** Aseptic laboratory technique: plating methods. JoVE 63: **e3063.** https://www.jove.com/t/3064/aseptic-laboratory-techniques-plating-methods.
35. **Chen., K., Han., B., Ma., X., Zhang., H., Meng., L., Wang., G., XiaF., Song., X., & Ling., S. (1999).** Establishment and preliminery use of hepatitis B virus pre S1/2 antigen assay. World Journal of Gastroenterology **5(6):550-552.** https://www.ncbi.nlm.nih.gov/pmc/articles/PMC4688807/.
36. **Stills., HF. (2005).** Adjuvants and antibody production: dispelling the myths associated with Freund's complete and other adjuvants. Ilar j **46(3): 280-293.** https://academic.oup.com/ilarjournal/article/46/3/280/739212.
37. **Jason., RC., Kathryn., B., Catherine., DJ., Vicki., C., John., BM. (2011).** Comparison of a bacteriophage-delivered DNA vaccine and acommercially available recombinant protein vaccine against hepatitis B. FEMS Immunol Med Microbiol, **61:197–204.** https://pubmed.ncbi.nlm.nih.gov/21204995/.
38. **Moore., RE. (2002).** Immunochemical methods. In: Mcclachey KD (ed), Clinical laboratory medicine, 2nd ed. Lippincott Williams & Wilkins.
39. **Sallam., KM., El-Bayoumy., ASA., and Mehany., NL. (2017).** Radioimmunochemical studies for the development of a solid-phase radioimmunoassay system using coated beads for the assessment of human chronic gonadotropin. Radiochemistry, **59(2): 181-187.** https://link.springer.com/article/10.1134/S1066362217020126.
40. **Minic., R., & Zivkovic., I. (2020).** Optimization, validation and standardization of ELISA. In *Norovirus*, London, UK: IntechOpen, **pp. 9-28.**
41. **El Kolaly., MT., Mehany., NL., Hassan., SEM., Ayyoub., SM. (2006).** Development, optimization and validation of 1-Step TSH IRMA using solid phase anti-TSH magnetic particles. Arab J Nucl Sci Appl **39: 320-333.** https://inis.iaea.org/search/search.aspx?orig_q=RN:37055663.
42. **Andreasson., U., Perret-Liaudet., A., Van., WVD., Blennow., L., Chiasserini., D., Engelborghs., S., Fladby., T., Genc., S., Kruse., N., Kuiperij., H., Kulic., L., Lewczuk., P., Mollenhauer., B., Parnetti., L., Vanmechelen., E., Verbeek., M., Winblad., B., Zetterberg., H., & Teunissen., C. (2015).** A Practical guide to immunoassay method validation. Frontiersin Neurology **6:179.** https://www.frontiersin.org/articles/10.3389/fneur.2015.00179/full.